AGU PUBLICATIONS

JGR

Journal of Geophysical Research: Solid Earth

RESEARCH ARTICLE
10.1002/2017JB015003

Key Points:
- Earthquakes associated with the 2008 Dallas-Fort Worth Airport sequence continued to migrate away from injection through 2015
- Pore pressure diffusion models indicate high-volume injection led to long-term stress changes that trigger earthquakes years after shut down
- Even brief periods of high-volume wastewater injection can perturb stress and lead to years of seismicity

Supporting Information:
- Supporting Information S1
- Data Set S1
- Data Set S2

Correspondence to:
P. O. Ogwari,
pogwari@mail.smu.edu

Citation:
Ogwari, P. O., DeShon, H. R., & Hornbach, M. J. (2018). The Dallas-Fort Worth Airport earthquake sequence: Seismicity beyond injection period. *Journal of Geophysical Research: Solid Earth*, *123*, 553–563. https://doi.org/10.1002/2017JB015003

Received 18 SEP 2017
Accepted 2 JAN 2018
Accepted article online 7 JAN 2018
Published online 26 JAN 2018

The Dallas-Fort Worth Airport Earthquake Sequence: Seismicity Beyond Injection Period

Paul O. Ogwari[1], Heather R. DeShon[1], and Matthew J. Hornbach[1]

[1]Department of Earth Science, Southern Methodist University, Dallas, TX, USA

Abstract The 2008 Dallas-Fort Worth Airport earthquakes mark the beginning of seismicity rate changes linked to oil and gas operations in the central United States. We assess the spatial and temporal evolution of the sequence through December 2015 using template-based waveform correlation and relative location methods. We locate ~400 earthquakes spanning 2008–2015 along a basement fault mapped as the Airport fault. The sequence exhibits temporally variable *b* values, and small-magnitude ($m < 3.4$) earthquakes spread northeast along strike over time. Pore pressure diffusion models indicate that the high-volume brine injection well located within 1 km of the 2008 earthquakes, although only operating from September 2008 to August 2009, contributes most significantly to long-term pressure perturbations, and hence stress changes, along the fault; a second long-operating, low-volume injector located 10 km north causes insufficient pressure changes. High-volume injection for a short time period near a critically stressed fault can induce long-lasting seismicity.

Plain Language Summary The 31 October 2008 earthquakes at the Dallas-Fort Worth International Airport were the first documented earthquakes in the Fort Worth Basin in the historic record and the first of multiple earthquake sequences in the basin associated with waste-fluid injection. Since the shut-in of the wastewater disposal well nearest to the initiation point of the sequence, seismicity has continued for more than 7 years over a 6 km long fault. We found that the high-volume brine injection well located within 1 km of the 2008 earthquakes, although only operating from September 2008 to August 2009, contributes most significantly to long-term pressure perturbations, and hence stress changes, along the fault. The high-volume injection for a short time period near a critically stressed fault can induce long-lasting seismicity.

1. Introduction

Post-2008 earthquake rate increases in the central United States have been associated with large-scale subsurface disposal of waste-fluids from oil and gas operations (e.g., Ellsworth, 2013; Rubinstein & Mahani, 2015; Walsh & Zoback, 2015; Weingarten et al., 2015). The 31 October 2008 earthquakes at the Dallas-Fort Worth International Airport (hereafter, DFW Airport) were the first documented earthquakes in the Fort Worth Basin (FWB) in the historic record (Frohlich et al., 2010, 2011, 2016; Frohlich & Davis, 2002) and the first of multiple earthquake sequences in the basin associated with waste-fluid injection (Frohlich, 2012; Hornbach et al., 2015, 2016; Justinic et al., 2013; Lund Snee & Zoback, 2016; Reiter et al., 2012; Scales et al., 2017; Weingarten et al., 2015). As efforts to design mitigation strategies for induced earthquakes continues, questions regarding the temporal continuity in rates and magnitudes during and after reduction or cessation of subsurface injection remain unclear (Bommer et al., 2015). Understanding the spatiotemporal evolution of induced earthquake sequences like those in the FWB provides data to inform mitigation strategies.

Seismicity at the DFW Airport began on 31 October 2008 with a series of 8 m_{blg} 2.6 to 3.0 earthquakes reported by the U.S. Geological Survey (USGS) National Earthquake Information Center (NEIC). Following the 31 October events, seismologists from Southern Methodist University (SMU) deployed six 3-component broadband seismographs and recorded 11 events of magnitude 1.7 to 2.3, including a cluster on 20 November not reported by the NEIC (Frohlich et al., 2010, 2011) (Figure 1). A m_{blg} 3.3 in May 2009 prompted redeployment of four stations around the airport. Analysis indicated that the earthquakes were located within a 1 km radius of a Class II saltwater disposal (SWD) well that had begun injecting 7 weeks prior to the October earthquakes (Figure 2). Reflection data showed a regional NE-SW trending normal fault (Railroad Commission of Texas, 2015), now called the Airport fault, present at earthquake and injection depths. The south airport well (hereafter, S-well) ceased injecting in August 2009. Frohlich et al. (2011)

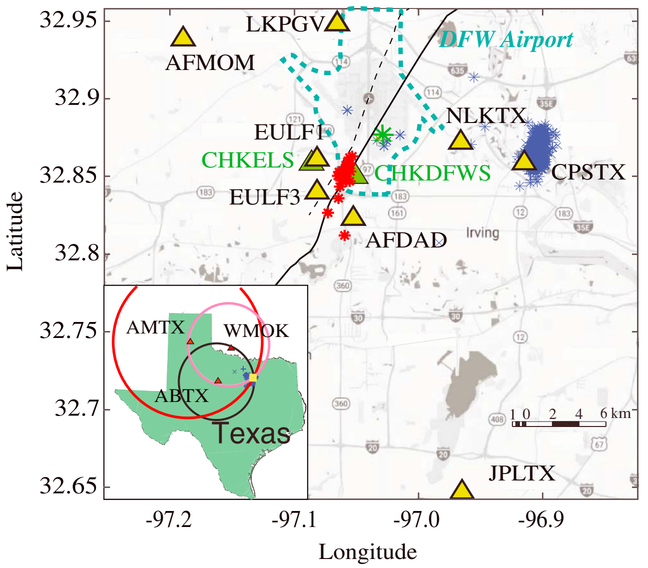

Figure 1. Study area for the DFW Airport earthquake sequence. The 2008–2009 SMU operated stations (yellow triangles), reanalyzed in this study, and recorded events (red asterisks) reported in Frohlich et al. (2010, 2011). Janská and Eisner (2012)reported additional events (hypocenters approximated by green asterisks) using stations operated by Chesapeake Energy (green triangles); CHKDFWS station is used in this study. Earthquakes reported by the 2013–2016 SMU earthquake catalog (blue asterisks) indicate continued seismicity at the DFW Airport (property boundary is dashed cyan line). The seismicity around station CPSTX is the Irving sequence. Regional normal faults mapped at the top of the Ellenburger formation are indicated by black lines (Railroad Commission of Texas, 2015). The solid black line is the Airport fault. Inset: Map of Texas showing the three regional seismic stations used in this study. The circles denote the equidistant circumference used for relocation methods described in the text.

concluded that the DFW Airport earthquakes were probably triggered on a preexisting fault by subsurface stress changes due to waste-fluid injection. Reiter et al. (2012) reanalyzed the data collected during the SMU deployment, were able to detect more events, and reached the same conclusion as Frohlich et al. (2011) regarding cause.

Beginning in 2009, temporary seismic stations were placed at the airport by Chesapeake Energy, which operated multiple production and two Class II SWD wells on the property (see Figure 2 for injection well locations). Janská and Eisner (2012)used these data to document a cluster of earthquakes about 4 km north of the S-well beginning in May 2010 through January 2012 (hypocenters approximated by green asterisks, Figure 1). Deployment of local seismic stations in the area by SMU, including redeployment of AFDAD in 2014, revealed small-magnitude earthquakes continued at the airport; earthquakes from 2013 to present are reported in the SMU local earthquake catalog (blue asterisks, Figure 1) (Hornbach et al., 2015; Magnani et al., 2017; Scales et al., 2017).

We hypothesize that migration of the earthquakes along the Airport fault follows diffusion of pore fluid pressure changes at depth due to injection of waste fluids at the airport injectors. In order to provide a more consistent understanding of the spatial and temporal evolution of the sequence, we reanalyze local seismic data and long-running regional stations to develop a spatially and temporally consistent earthquake catalog (Figure 1, inset). We use the NEIC and local earthquake catalogs as detection templates for cross correlation of continuous waveform data at regional stations that recorded from 2008 to 2015. We employ a novel relative location technique to constrain epicentral location using regional data. We model the pore pressure changes in the Ellenburger formation that is targeted for waste-fluid injection and in the Precambrian crystalline basement over the period of injection to December 2015 and consider pressure influences from both the south and north injection wells located at the airport (Figure 2).

2. The Revised DFW Airport Catalog

2.1. Template Earthquakes

Recording earthquakes at the DFW Airport illustrates one of the general challenges of studying induced earthquakes in the central United States—namely, a space and time bias exists in network coverage that limits the ability to capture the initial onsets of the earthquake sequences and constrain sequence history. Prior to 2008, the nearest seismic station to the DFW Airport was WMOK at a distance of 264 km (Figure 1), and only regional stations AMTX and ABTX provide high signal-to-noise broadband coverage of most of the DFW Airport sequence (Figure S1 in the supporting information). SMU and Chesapeake deployed seismometers in and around the airport, but operation times varied (Figure S1).

We analyze data from the SMU networks and CHKDFWS to build a revised local earthquake catalog specific to the DFW airport sequence (Data Set S1). *P* and *S* phase onsets are manually identified, and earthquakes are located using GENLOC (generalized earthquake-location) algorithms (Pavlis et al., 2004) within the Antelope database management system (Kinemetrics, Inc.) combined with the 1-D velocity model used by Frohlich et al. (2011) derived from the Trigg well velocity log (Geotechnical Corporation, 1964). We reproduce the Frohlich et al. (2011) catalog and add 19 earthquakes ranging in depth between 2.8 and 5.0 km. Eight events reported by Janská and Eisner (2012) study are detected but cannot be located because we did not have access to all Chesepeake seismic stations. The revised local catalog totals 33 earthquakes. Crustal phases (*Pg* and *Lg*) at WMOK, ABTX, and AMTX for events in the revised local catalog recorded at regional distances and all unique NEIC catalog events are manually picked, resulting in 38 template earthquakes (Data Set S2, denoted by an asterisk).

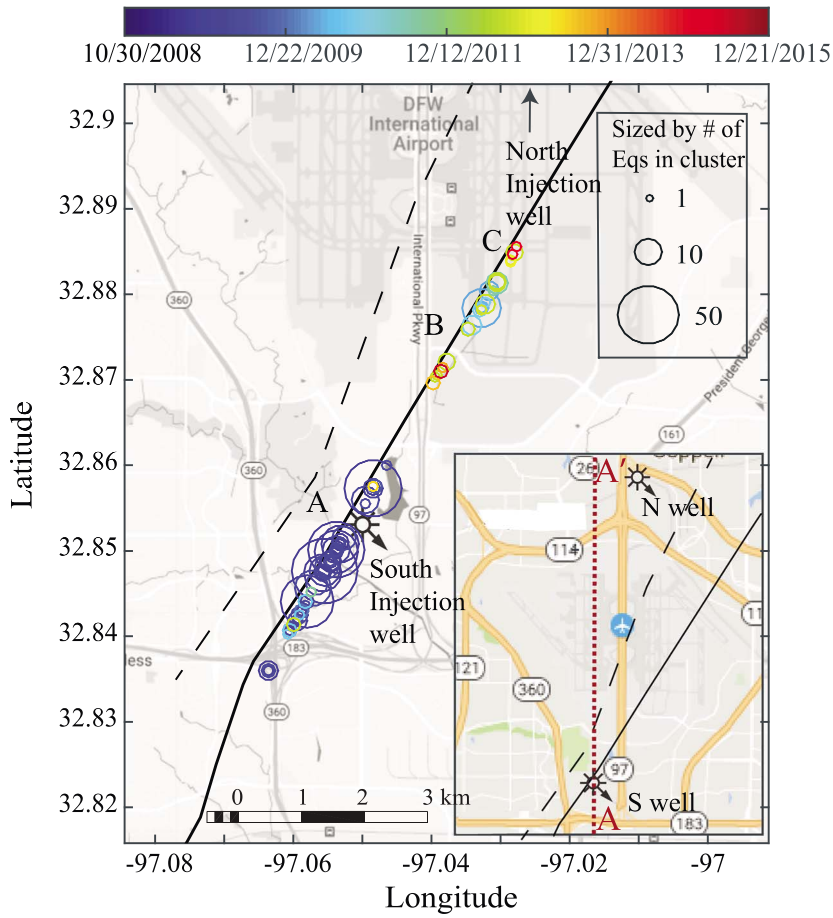

Figure 2. Spatiotemporal clustering of earthquakes sized by the number of events in a cluster. Clusters are binned per month and are colored based on time. The solid black line is the Airport fault, and the dashed line is unnamed (Railroad Commission of Texas, 2015). The north injection well is 7.5 km north of the point C. Inset: Location of the north (N) and south (S) injection wells relative to the DFW Airport. The dashed red line coincides with the pore pressure diffusion model cross section shown in Figure S5.

2.2. Matched-Filter Detection and Clustering Analysis

Lg phase templates are used in a matched-filter analysis applied to continuous horizontal data from WMOK, ABTX, and AMTX recorded between January 2008 and December 2015. The time window is set to 10 s before and 20 s after *Lg* onset, data are band-pass filtered between 0.5 and 5 Hz, and cross correlation is computed within the GISMO toolbox for MATLAB (Reyes & West, 2011). Initial detection of a new earthquake occurs when both horizontal channels have identical trigger times and a correlation coefficient (CC) $>$ 0.64. This minimum correlation threshold is set based on manual review that positive detections on the regional stations are associated with *P* and/or *S* arrivals one at least one local station. However, we found the 0.64 CC threshold still produces positive detections corresponding to events associated with the 2013–2014 Azle (Hornbach et al., 2015) and 2014 to present Irving-Dallas (Magnani et al., 2017) earthquake sequences. In other words, at regional distances between 0.5 and 5 Hz, the DFW Airport earthquake *Lg* templates positively correlate with *Lg* waves from earthquakes occurring at faults located 50 km west (Azle) and 12 km east (Irving-Dallas) of the Airport fault.

In order to distinguish the DFW Airport sequence from other sequences, we implement an additional clustering analysis step using the CC coefficients. Spatial clusters are identified using a dendrogram-based hierarchical pair-group clustering algorithm (Reyes & West, 2011, and references therein). Clusters of highly similar events are formed based on highest mean CC coefficient of the event or cluster pairs. We choose a correlation threshold of 0.85 based on visual inspection of the waveform attributes

(Figure S2). Finally, we examine the clusters independently identified at the three regional stations to confirm that the DFW Airport events separate from the Azle and Dallas-Irving sequences. This procedure results in an additional 374 earthquakes, bringing the total data set to 412 events (Data Set S2). For earthquakes identified via matched-filter approaches, we calculate a magnitude (*M*) based on the relative amplitudes of the newly located events to those reported in the USGS catalog. The magnitude calculation is determined by regressing the logarithm of the peak horizontal amplitude at WMOK and ABTX separately (Figure S3) and applying the resulting function to the new events. For each event, magnitude pairs are compared the variance to ascertain the consistency in magnitude determination.

2.3. Earthquake Location Using Regional Differential Times

We apply a equal differential time (EDT) method as presented by Font et al. (2004) that is based on the master station method by Zhou (1994). The technique has been modified to use a reference hypocenter in addition to a traditional reference station (here, WMOK) to take advantage of both station-pair and event-pair differential time data. This enables location of earthquakes with undetermined origin time and reduces location uncertainties by using prelocated reference events for calibration. Applying the concept of double-pair double difference location method (Guo & Zhang, 2017), for a given absolute location of event *i*, the difference between the arrival time, *A*, of events *i* and *j* at stations *l* and *k* can be expresses as follows:

$$\left(A_l^i - A_k^i\right) - \left(A_l^j - A_k^j\right) = \left(\Sigma_{m=1}^3 \left(\frac{\partial C_l^i}{\partial x_m^i} - \frac{\partial C_k^i}{\partial x_m^i}\right) dx_m^i - \Sigma_{m=1}^3 \left(\frac{\partial C_l^j}{\partial x_m^j} - \frac{\partial C_k^j}{\partial x_m^j}\right) dx_m^j\right)^{\mathrm{cal}} = \left(D_{lk}^{ij}\right)^{\mathrm{cal}}, \quad (1)$$

where C is the calculated traveltime and D^{cal} is the calculated difference between the EDT surfaces for any event pair and station pair. The complete derivation of equation (1) is shown in Text S1. Due to the limited number of station pairs for the DFW Airport sequence, the technique only results in relative epicenters and depth cannot be sufficiently resolved. We therefore fix depth for all events to 4.4 km based on the mean depth in the local catalog and assume the event-pair differential times represent epicentral difference (see discussion in Text S1). Only earthquakes with *Pg* or *Lg* waves recorded at all three regional stations, and hence having two equal station-pair differential times (Figure S4), can be relocated relative to the master hypocenter (Data Set S2, 111 earthquakes denoted with DF). We assign locations to the remaining 302 very small earthquakes by taking advantage of the prior clustering analysis. Each of the 111 relocated earthquakes participates in a cluster and is used to define the reference cluster location, then propagated to all unrelocated members of the cluster; if more than one relocated earthquake is associated with a cluster, the mean epicenter of the relocated events is assigned as the reference cluster location (Data Set S2). Formal uncertainties are not calculated, but for clusters containing multiple relocated events, the largest epicentral difference is 0.52 km, which is taken as an estimate of location uncertainty.

3. Pore Pressure Diffusion Model Methodology

We determine pore pressure effects in the subsurface generated by the injection of the two wells by developing a 3-D pore pressure diffusion model that incorporates all first-order regional stratigraphy and mapped faults (Figure S5). The model consists of a more permeable (5×10^{-14} m^2) Ellenburger formation, where injection occurs, situated between two comparatively less permeable formations—the Barnett shale (1×10^{-18} m^2) above and granitic basement below (1×10^{-19} m^2) (Hornbach et al., 2015; Loucks et al., 2009). Ellenburger thickness is defined by regional stratigraphy and well logs. The fault width is approximated to 10 m based on the approximate displacement in the regional faults that is in tens of meters (Magnani et al., 2017; Scales et al., 2017). Fault width has been found to be directly proportional to the fault displacement (Mitchell & Faulkner, 2009; Savage & Brodsky, 2011). The faults are assigned a uniform permeability in the range of 1×10^{-13} m^2 and 1×10^{-14} m^2 to test the influence of permeability of the fault and the Ellenburger on pore pressure diffusion in the basement (Figure S6). The upper margin of fault permeability is set higher than the surrounding country rock to define a critically stressed fault (Barton et al., 1995) while the lower margin defines a sealed fault.

We compute the 3-D numerical model using MODFLOW-2005, a modular finite-difference code developed at the USGS that implements the partial differential equation of groundwater flow as (Harbaugh, 2005)

$$\frac{\partial}{\partial x}\left\{K_{xx}\frac{\partial h}{\partial x}\right\}+\frac{\partial}{\partial y}\left\{K_{yy}\frac{\partial h}{\partial y}\right\}+\frac{\partial}{\partial z}\left\{K_{zz}\frac{\partial h}{\partial z}\right\}=S_s\frac{\partial h}{\partial t}-W, \tag{2}$$

where K_{xx}, K_{yy}, and K_{zz} are the hydraulic conductivity values along the x, y, and z coordinate axis with the dimensions of length (L) divided by time (T), h is the hydraulic potential head (L), S_s is the specific storage (L^{-1}) herein assigned as 7.3×10^{-6} m^{-1} (Hornbach et al., 2015), and W is the volumetric flux per unit volume (T^{-1}). The model domain is 40 × 40 km in the horizontal plane with the surface grid discretization varying between approximately 10 m in proximity of the injection wells and the main faults, to approximately 150 m near the model boundaries with layer thickness discretization of 200–400 m. The model top is set to ground surface, while the base of the model is defined at 8 km (Figure S5). Flow across the lateral model boundaries is simulated via head-dependent flux boundaries. We define the injection interval for northern injector well (N-well) and the southern injector well (S-well) from 3,636 to 3,938 m and 3,124 to 4,184 m respectively, based on the reported interval depths provided by the Railroad Commission of Texas H-10 reports (see Text S2). Wastewater disposal at the south well began in September 2008 and averaged approximately 50,000 m^3 per month until August 2009 when the well was shut in. At the north well, injection began in November 2007; peak monthly rates of 68,000 m^3 per month were achieved in March 2008; since 2009 injection rates have decreased and were at about 10,000 m^3 per month at the end of 2015. We run the model for a 9 year period starting September 2007 and test the influence of hydrological properties of the Ellenburger and the faults (see Figure S6).

4. Results

4.1. Earthquake Location

Seismicity begins on 30 November 2008 southwest of the S-well and migrates northeast of the well over the next 7 years (Figure 2). Detectable events occur in discrete clusters in time and space rather than continuously. The first cluster, consisting of 192 recorded earthquakes (the largest a m_{blg} 2.8), occurs near point A between 30 October and 5 November 2008 and within 1 km of the S-well. Most events during this period are located SW of the S-well where the spatial density of seismicity is more than double that of the area NE of the well. The next earthquake clusters occur on 20 November 2008 (Frohlich et al., 2011), 26 December 2008, and between 15 and19 May 2009. The first 7 months of seismic activity account for ~80% of the earthquakes in the expanded DFW Airport catalog, with all events located within 1 km of the S-well.

Starting 24 May 2010, however, the earthquakes migrate ~2 km to the northeast (point B in Figure 2) before reoccurring again in October and November 2010 at the southern edge of the fault section where the first cluster was located (point A). For each of these clusters, earthquakes align along the same fault system (Railroad Commission of Texas, 2015) but at greater distances from the injector site and the 2008 earthquake cluster. In September 2012, the area between the S-well and point B (~1.5 km to the northeast) experiences seismicity, indicating continued seismicity northeast of the well. The largest event in the sequence reported in the NEIC catalog as m_{blg} 3.4 occurs on 30 September 2012 and is located midway between points B and C. By July 2015, the earthquakes have occurred along ~80% of the ~6 km long fault with the latest events (red in Figure 2) recorded by the SMU ZW network. Although all earthquakes generally occur in clusters, seismicity rates drop after May 2010, averaging 1 event per month compared to the 23 events per month in 2008–2009 period.

4.2. Magnitude-Frequency Distribution

Earthquake magnitudes range from 0.5 to 3.4, and the expanded DFW Airport catalog exhibits a magnitude of completeness (Mc) of 1.9 determined using the maximum curvature algorithm (Wiemer & Wyss, 2000). The catalog is dominated by the initial 2 months of earthquakes located within 1 km of the S-well that are characterized by low magnitudes ($M < 2$) (Figure 3). We therefore also analyze the first 2 months of seismicity separately from the rest of the catalog. The first 2 months have a convex-type distribution due to deficiency of larger earthquakes ($M > 2.8$) reported in the later period. On this data set we apply an upper-truncated power law (Utsu, 1978) with a magnitude bin size of 0.1 to determine the b value. The upper-truncated power law describes a convex-type distribution of magnitude frequency where the linear Gutenberg-Richter

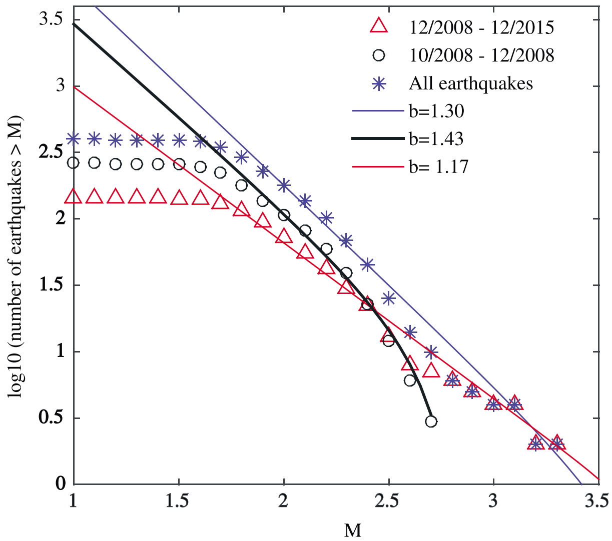

Figure 3. The Gutenberg-Richter magnitude-frequency plot for earthquakes occurring in the first 2 months (black), the rest of the period (red), and the entire sequence (blue). Estimated b values shown in the top right have been computed using 164, 94, and 229 earthquakes in the first 2 months, the rest of the period, and the entire sequence, respectively.

relationship does not fit the data set. For the later period and the entire data set, we compute b values using the maximum-likelihood method (Aki, 1965; Bender, 1983) with a magnitude bin size of 0.1 (Figure 3), though we recognize that the total number of earthquakes is low for this statistical approach. The catalog exhibits a time-variant b value distribution. The initial 2 months of the sequence has Mc of 1.8 and a b value of 1.43 with $\sigma = 0.0461$ and a truncation magnitude of $M = 2.75$. Truncation magnitude is defined herein as the maximum magnitude within a data set. The remainder of the catalog has a Mc of 1.9 and a b value of 1.17 with $\sigma = 0.1129$. The b value is 1.3 for the entire data set with $\sigma = 0.0709$. The b values are consistent with the 1.3 estimate by Frohlich et al. (2011) based on analysis of the initial 8 months of seismicity and the b value estimate of 1.1 reported by Janská and Eisner (2012) based on earthquakes occurring between October 2009 and January 2012.

4.3. Pore Pressure Diffusion

We analyze model-predicted pore pressure change in the basement (4.4 km depth) at three areas along the fault based on the spatiotemporal migration of seismicity. We present pore pressure change (Figure 4) around the well (point A) where the DFW Airport earthquakes initiate in 2008, around the location of the May 2010 earthquakes (point B), and at the northern edge of the seismicity (point C). Pore pressure increase along the faults in the basement occurs at varying rates depending on the distance from the injection point, rate and timing of injection, and the

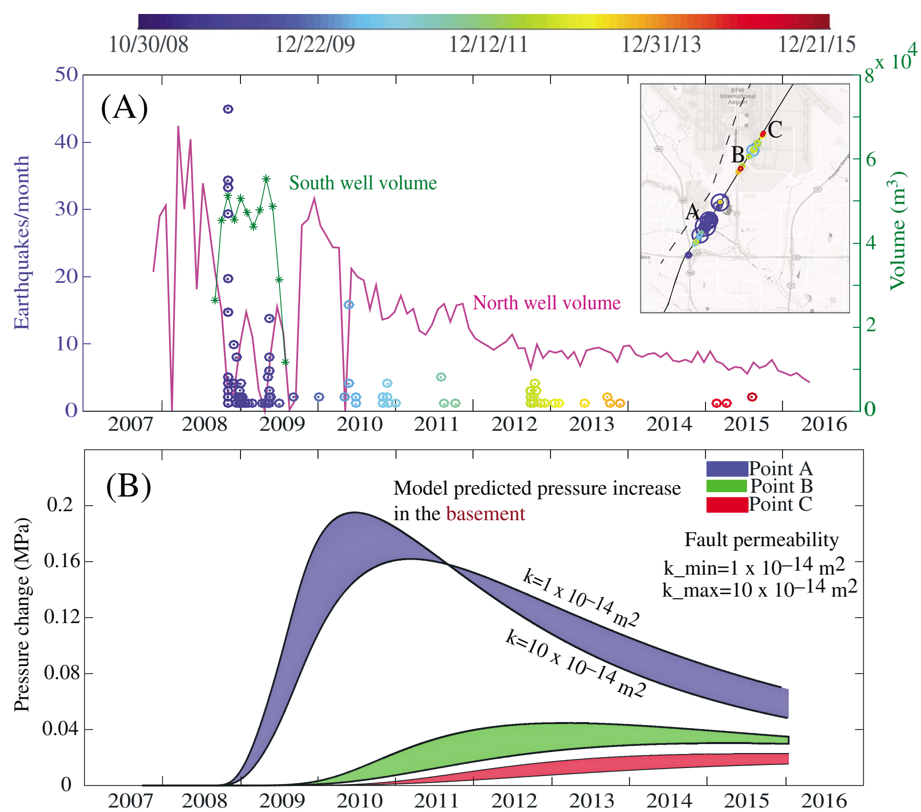

Figure 4. (a) Monthly rate of seismicity over 7 year period and monthly rate of injection at the closest wells and (b) the predicted pore pressure chance in the crystalline basement for a range of fault permeability. Pore pressure is predicted at points A, B, and C (inset in Figure 4a).

hydraulic permeability of the fault, where modeling indicates most of the pressure change is channeled. The pore pressure increases at a higher rate around the injection point and the rate reduces with distance from the point of injection but shows the most significant change in pressure between the fault and the surrounding country rock. Pore pressure increases faster and peaks higher in the more permeable fault with a faster decay rate than in the less permeable fault. For the permeability range defined on the fault, pore pressure change around the S-well is 0.0008–0.0012 MPa at the start of seismicity and peaks between 0.18 and 0.2 MPa approximately 2–2.5 years after start of injection in the S-well. At points B and C, the pore pressure peak range is 0.03–0.044 MPa and 0.016–0.022 MPa, respectively, with pressures peaking 4.5 to 6.5 years (point B) and over 7 years (point C) after S-well injection begins.

5. Discussion

DFW Airport earthquakes begin in late October 2008 and extend through August 2015. Analysis of the regional data at WMOK and AMTX indicates no earthquakes greater than magnitude 1.8 occurred within the basin between 1 January and 29 October 2008. We successful identify events reported by previous studies (e.g., Frohlich et al., 2011; Janská & Eisner, 2012) and additionally expand the total number of reported earthquakes by nearly three times through incorporation of additional stations and template-matching approaches. The expanded DFW Airport catalog is a more complete data set that allows us to analyze the spatiotemporal evolution of seismicity on the Airport fault.

5.1. SW to NE Earthquake Migration

Spatiotemporal migration of earthquakes away from the injection point in a postinjection period is not unique to DFW Airport sequence. Such migration has previously been observed in the enhanced geothermal field of Basel, Switzerland, but on a smaller temporal (days) and spatial (×100 m) scale (Bachmann et al., 2011). One interpretation of migrating seismicity is that it indicates propagation of the triggering process along a seismogenic fault that is favorably oriented. The duration and the area of influence of postinjection seismicity is partly dependent on the diffusivity of the host formation and magnitude of increased pore pressure. Similar to the DFW Airport seismicity, Hsieh and Bredehoeft (1981) documented seismic activity associated with injection at the Rocky Mountain Arsenal to have continued at least 7 years following shut-in. Within 14 months of the shut-in at the Rocky Mountain Arsenal, the Denver area experienced three $M_w > 5$ events, which were, in fact, the largest events of that sequence. Another comparable case is the Castor project in Spain, where the largest event (M_w 4.3) occurred about 2 months into the postinjection period (Gaite et al., 2016). Similarly, the largest event of the DFW Airport sequence, a m_{blg} 3.4, occurred 3 years after injection ceased at S-well. Even though the duration of injection was shorter at the DFW Airport than at the Rocky Mountain Arsenal, the DFW Airport sequence continued for at least 6 years since injection at the south well ceased. In both instance, high rates of injection over short time periods (days to months) induced earthquakes that continued years after injection ceased. Seismicity can be attributed to continued pressure diffusion along critically stressed faults combined with low diffusivity of the crystalline basement. This implies that even very brief periods of injection (months), as opposed to years as in the cases of Rocky Mountain Arsenal can result in years of seismicity in a region.

Not all cases of induced seismicity with a documented well shut-in have produced their largest event in their postinjection period. The Guy-Greenbrier Arkansas sequence had its largest event during its injection period and, as in the Castor project, the postinjection seismic activity is constrained within the coinjection active zone (Horton, 2012).

5.2. Time-Dependent Magnitude-Frequency Relationship

The Gutenberg-Richter relationship has characteristic truncation magnitude observed from other studies of induced seismicity. The DFW Airport sequence has a truncation magnitude of 2.75 during the first 2 months of seismicity with the rest of the period having a maximum magnitude of 3.4. In Basel, Bachmann et al. (2011) found that the coinjection period exhibited characteristically lower truncation magnitude (~2) compared to the postinjection data (~3). Similar truncation magnitude differences were observed in Castor, Spain (Cesca et al., 2014). This characteristic lower coinjection truncation magnitude has been attributed to the an unproportionally high rate of small earthquakes during the injection period (Segall & Lu, 2015). An increased proportion of smaller earthquakes was also observed in Guy-Greenbrier sequence during wastewater injection (Ogwari et al., 2016). In the three cases, the events producing lower truncation magnitude were located within hundreds of meters from the injection well where pressure is highest.

We postulate the lack of higher-magnitude events near the S-well during the initial period of injection is due to high-rate pore pressure increase. The rate of pressurization in a high-rate injection well is highest near the injection point and decreases with distance farther from the injection point. Higher pressurization rates have been found to lead to higher breakdown pressure in hydraulic fracturing process (Haimson & Zhao, 1991), which in turn have produced inversely proportional fracture lengths (Stoeckhert et al., 2015). Since the moment release of an earthquake is a function of the fault area, higher pressurization rates induce microseisms that are constrained within the region of pressurization. The inverse implies that lower pressurization rates could effectively distribute pore pressure increases over a larger area, thereby subjecting multiple faults or a larger area on any given fault to the equal rates of pore pressure increase. Increasing pore pressure over a larger fault area could trigger relatively larger events on an already critically stressed fault.

The initial first 2 months of seismicity for the DFW Airport sequence produces a *b* value of 1.43, similar to the first 2 months of the Guy-Greenbrier sequence where the earthquakes were concentrated within 1 km radius of the injection well (Mousavi et al., 2017). The overall *b* value of 1.3 is in the range values documented in enhanced geothermal systems (Albaric et al., 2014; Bachmann et al., 2011; Baria et al., 1999; Häring et al., 2008) where injection occurs at elevated pressures. However, it remains higher than values reported in other wastewater disposal cases (Ake et al., 2005; Justinic et al., 2013; Ogwari et al., 2016) and lower than those recorded in hydraulic fracturing processes (Vermylen & Zoback, 2011; Zhou et al., 2013). At the later period, the *b* value reduces toward a unit value as experienced in postinjection period of the Basel sequence (Bachmann et al., 2011), an indication of low-rate pore pressure change.

5.3. Pore Pressure Diffusion

A combination of injection well proximity to a fault and fault orientation plays a major role in inducing the DFW Airport earthquakes. For the N-well, our modeling suggests that the ~3 km offset distance from the active fault and lower injection pressure limits pressure communication to the crystalline basement and thus produces no spatially associated earthquakes. The N-well operation starts 10 months earlier than the S-well at a comparable rate but at less than half the injection pressure. Although injection at N-well continued at a decreasing rate over the duration of seismicity, the spatiotemporal occurrence of earthquakes fits the modeled pressure diffusion primarily contributed by the S-well (Figures 5 and S6). The nearest documented fault (~1 km) to the N-well is subparallel to the maximum horizontal stress, which is oriented at ~N020°E in the FWB (Lund Snee & Zoback, 2016). The orientation and location of this nearest fault is not consistent with the location of seismicity but is optimally oriented for failure only from latitude N32.86 to N32.835. The bend in the Airport fault SE of the S-well results in an unfavorable orientation relative to the maximum horizontal stress, which explains the absence of continued SE migration during and after injection.

On the other hand, injection at a similar rate in the S-well over a short period near a critically stress fault leads to earthquakes occurring over 7 years. Once the pore pressure has been elevated in the crystalline basement, the pressure decay and diffusion is dependent on the diffusivity in the basement. Over time, pore pressures continue to gradually increase away from the injection point at a lower rate and absolute value. Inducing earthquakes on a critically stressed fault may take as little as 0.001 MPa pressure increase (Rothert & Shapiro, 2007). The modeled pore pressure results for the range of permeabilities used are at least 1 order of magnitude higher than the Rothert and Shapiro (2007) lower boundary and consistent with the range predicted at similar induced seismicity sites in Texas (Hornbach et al., 2015, 2016). Thus, first-order modeling results indicate seismicity occurring northeast of the S-well along years after injection represents a plausible explanation for these earthquakes.

6. Conclusions

The Dallas-Fort Worth Airport earthquakes have continued to occur since the first recorded event on 31 October 2008. A combination of template matching, hierarchical clustering, and differential traveltimes have produced 412 earthquake epicenters that generally migrate from SW to NE over time, over 80% of a 6 km long fault. Earthquakes have migrated away from the S-well in both direction along the fault with time; however, more seismicity has occurred toward the northeast, where the fault is best oriented for failure in the

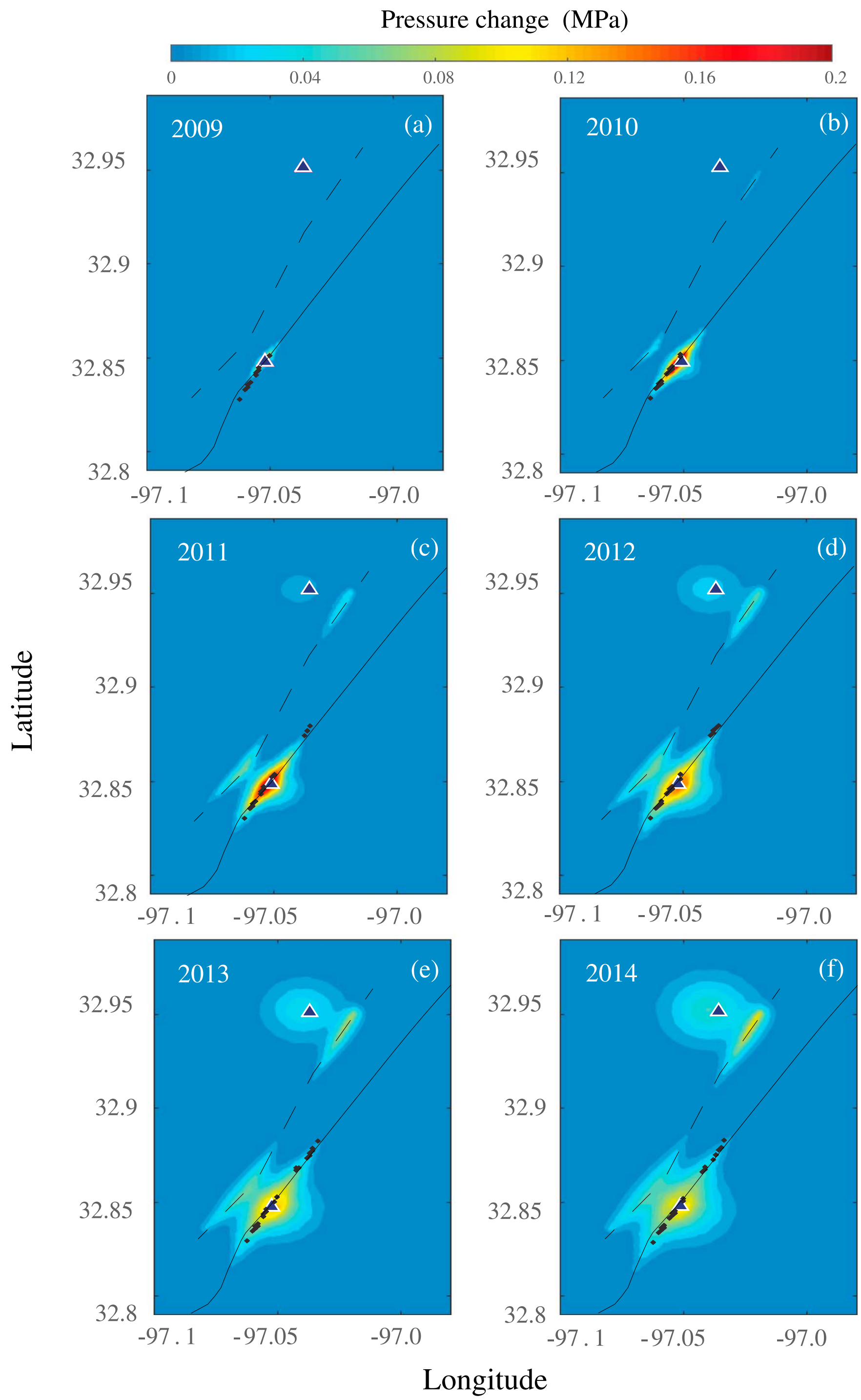

Figure 5. Map view of predicted pore pressure change in the basement at ~4.4 km depth in the month of March of each year from 2009 to 2014. The permeability of the Ellenburger in the model is set at 5×10^{-14} m^2 with a uniform faults' permeability of 1×10^{-13} m^2 pressure from the N-well has minimal contribution to pressure change in the Airport fault. The closest fault to the N-well experiences pressure increase in the range of 0.01–0.1 MPa between 2011 and 2015, but it is not optimally oriented to the maximum horizontal stress. The black dots are the cumulative earthquakes at the time of the predicted pore pressure change.

modern stress regime (Lund Snee & Zoback, 2016). Seismicity peaks at the beginning of the sequence and decays over time with earthquakes occurring in discrete clusters in time and space rather than continuously in either. The initial high rate of low-magnitude earthquakes is consistent with, and likely the result of, elevated high-rate changes in injection pressure, similar to enhanced geothermal systems. Pore pressure modeling indicates that the S-well, though injecting for only 12 months but at high volume and rates in close proximity to a near critically stressed fault, causes spatiotemporal pressure changes into the crystalline basement most consistent with seismicity migration along the Airport fault. The modeling suggests that the high rate and volume S-well is the primary driver of seismicity and that the low- to moderate-rate injector to the north (the N-well) has had less effect on pore pressures within the basement. We conclude that it is therefore possible to induce small-magnitude earthquakes on a critically stressed fault over a longer time period (7 years) and farther distances (6 km) than previously documented in the FWB, even when the causative well is no longer injecting. The unfavorable orientation of the Airport fault south of the sequence limits migration of earthquakes to the SW. The observation that such a short period (12 months) of high injection triggers years of earthquakes is important as it suggests that even limited injection at high volumes and rates can lead to years of fault reactivation that extends several kilometers away.

Acknowledgments
Waveforms from SMU operated networks are archived at the IRIS Data Management Center under International Federation of Digital Seismic Network (FDSN) 2008-2009 X9 (doi:10.7914/SN/X9_2008) and FDSN 2013-2017 ZW (doi:10.7914/SN/ZW_2013). WMOK, AMTX, and ABTX are archived at IRIS under U.S. National Seismic Network (doi:10.7914/SN/US) or Transportable Array (doi:10.7914/SN/TA). We thank Cliff Frohlich and Brian Stump for critical reviews of early version of the manuscript. We also thank the Associate Editor and two anonymous reviewers for their comments and suggestions, which helped to strongly improve the manuscript quality. Research and data collection was partially supported by United States Geological Survey Earthquake Hazards Program Cooperative Agreement G15C00141 and G16AC00247 to H. R. D. and through the support of internal SMU funds.

References

Ake, J., Mahrer, K., O'Connell, D., & Block, L. (2005). Deep-injection and closely monitored induced seismicity at Paradox Valley, Colorado. *Bulletin of the Seismological Society of America*, *95*(2), 664–683. https://doi.org/10.1785/0120040072

Aki, K. (1965). Maximum likelihood estimate of b in the formula $\log(N)=a-bM$ and its confidence limits. *Bulletin. Earthquake Research Institute, University of Tokyo*, *43*, 237–239.

Albaric, J., Oye, V., Langet, N., Hasting, M., Lecomte, I., Iranpour, K., … Reid, P. (2014). Monitoring of induced seismicity during the first geothermal reservoir stimulation at Paralana, Australia. *Geothermics*, *52*, 120–131. https://doi.org/10.1016/j.geothermics.2013.10.013

Bachmann, C. E., Wiemer, S., Woessner, J., & Hainzl, S. (2011). Statistical analysis of the induced Basel 2006 earthquake sequence: Introducing a probability-based monitoring approach for Enhanced Geothermal Systems. *Geophysical Journal International*, *186*(2), 793–807. https://doi.org/10.1111/j.1365-246X.2011.05068.x

Baria, R., Baumgärtner, J., Gérard, A., Jung, R., & Garnish, J. (1999). European HDR research programme at Soultz-sous-Forêts (France) 1987–1996. *Geothermics*, *28*(4-5), 655–669. https://doi.org/10.1016/S0375-6505(99)00036-X

Barton, C. A., Zoback, M. D., & Moos, D. (1995). Fluid flow along potentially active faults in crystalline rock. *Geology*, *23*(8), 683–686. https://doi.org/10.1130/0091-7613(1995)023%3C0683:FFAPAF%3E2.3.CO;2

Bender, B. (1983). Maximum likelihood estimation of b values for magnitude grouped data. *Bulletin of the Seismological Society of America*, *73*(3), 831–851.

Bommer, J. J., Crowley, H., & Pinho, R. (2015). A risk-mitigation approach to the management of induced seismicity. *Journal of Seismology*, *19*(2), 623–646. https://doi.org/10.1007/s1095

Cesca, S., Grigoli, F., Heimann, S., González, A., Buforn, E., Maghsoudi, S., … Dahm, T. (2014). The 2013 September–October seismic sequence offshore Spain: A case of seismicity triggered by gas injection? *Geophysical Journal International*, *198*(2), 941–953. https://doi.org/10.1093/gji/ggu172

Ellsworth, W. L. (2013). Injection-induced earthquakes. *Science*, *341*(6142), 1225942. https://doi.org/10.1126/science.1225942

Font, Y., Kao, H., Lallemand, S., Liu, C. S., & Chiao, L. Y. (2004). Hypocentre determination offshore of eastern Taiwan using the maximum intersection method. *Geophysical Journal International*, *158*(2), 655–675. https://doi.org/10.1111/j.1365-246X.2004.02317.x

Frohlich, C. (2012). Two-year survey comparing earthquake activity and injection-well locations in the Barnett Shale, Texas. *Proceedings of the National Academy of Sciences of the United States of America*, *109*(35), 13,934–13,938. https://doi.org/10.1073/pnas.1207728109

Frohlich, C., & Davis, S. D. (2002). *Texas earthquakes* (Vol. 2). University of Texas Press.

Frohlich, C., Potter, E., Hayward, C., & Stump, B. (2010). Dallas-Fort Worth earthquakes coincident with activity associated with natural gas production. *The Leading Edge*, *29*(3), 270–275. https://doi.org/10.1190/1.3353720

Frohlich, C., Hayward, C., Stump, B., & Potter, E. (2011). The Dallas–Fort Worth earthquake sequence: October 2008 through May 2009. *Bulletin of the Seismological Society of America*, *101*(1), 327–340. https://doi.org/10.1785/0120100131

Frohlich, C., DeShon, H., Stump, B., Hayward, C., Hornbach, M., & Walter, J. I. (2016). A historical review of induced earthquakes in Texas. *Seismological Research Letters*, *87*(4), 1022–1038. https://doi.org/10.1785/0220160016

Gaite, B., Ugalde, A., Villaseñor, A., & Blanch, E. (2016). Improving the location of induced earthquakes associated with an underground gas storage in the Gulf of Valencia (Spain). *Physics of the Earth and Planetary Interiors*, *254*, 46–59. https://doi.org/10.1016/j.pepi.2016.03.006

Geotechnical Corporation (1964). Deep-hole site report, Trigg no. 1, Dallas County, Texas, *Geotechnical Corporation Technical Report 64–100*.

Guo, H., & Zhang, H. (2017). Development of double-pair double difference earthquake location algorithm for improving earthquake locations. *Geophysical Journal International*, *208*(1), 333–348. https://doi.org/10.1093/gji/ggw397

Haimson, B. C., & Zhao, Z. (1991). Effect of borehole size and pressurization rate on hydraulic fracturing breakdown pressure. In J.-C. Roegiers (Ed.), *Rock mechanics as a multidisciplinary science* (pp. 191–199). Rotterdam: Balkema.

Harbaugh, A. W. (2005). *MODFLOW-2005, the US Geological Survey modular ground-water model: The ground-water flow process* (p. 6-A16). Reston, VA: US Department of the Interior, US Geological Survey.

Häring, M. O., Schanz, U., Ladner, F., & Dyer, B. C. (2008). Characterisation of the Basel 1 enhanced geothermal system. *Geothermics*, *37*(5), 469–495. https://doi.org/10.1016/j.geothermics.2008.06.002

Hornbach, M. J., DeShon, H. R., Ellsworth, W. L., Stump, B. W., Hayward, C., Frohlich, C., … Luetgert, J. H. (2015). Causal factors for seismicity near Azle, Texas. *Nature Communications*, *6*, 6728. https://doi.org/10.1038/ncomms7728

Hornbach, M. J., Jones, M., Scales, M., DeShon, H. R., Magnani, M. B., Frohlich, C., … Layton, M. (2016). Ellenburger wastewater injection and seismicity in North Texas. *Physics of the Earth and Planetary Interiors*, *261*, 54–68. https://doi.org/10.1016/j.pepi.2016.06.012

Horton, S. (2012). Disposal of hydrofracking waste fluid by injection into subsurface aquifers triggers earthquake swarm in central Arkansas with potential for damaging earthquake. *Seismological Research Letters*, *83*(2), 250–260. https://doi.org/10.1785/gssrl.83.2.250

Hsieh, P. A., & Bredehoeft, J. D. (1981). A reservoir analysis of the Denver earthquakes: A case of induced seismicity. *Journal of Geophysical Research*, *86*(B2), 903–920. https://doi.org/10.1029/JB086iB02p00903

Janská, E., & Eisner, L. (2012). Ongoing seismicity in the Dallas-Fort Worth area. *The Leading Edge*, *31*(12), 1462–1468. https://doi.org/10.1190/tle31121462.1

Justinic, A. H., Stump, B., Hayward, C., & Frohlich, C. (2013). Analysis of the Cleburne, Texas, earthquake sequence from June 2009 to June 2010. *Bulletin of the Seismological Society of America*, *103*(6), 3083–3093. https://doi.org/10.1785/0120120336

Loucks, R. G., Reed, R. M., Ruppel, S. C., & Jarvie, D. M. (2009). Morphology, genesis, and distribution of nanometer-scale pores in siliceous mudstones of the Mississippian Barnett Shale. *Journal of Sedimentary Research*, *79*(12), 848–861. https://doi.org/10.2110/jsr.2009.092

Lund Snee, J. E., & Zoback, M. D. (2016). State of stress in Texas: Implications for induced seismicity. *Geophysical Research Letters*, *43*, 10,208–10,214. https://doi.org/10.1002/2016GL070974

Magnani, M. B., Blanpied, M. L., DeShon, H. R., & Hornbach, M. J. (2017). Discriminating between natural vs. induced seismicity from long-term deformation history of intraplate faults. *Science Advances*, *3*(11), e1701593. https://doi.org/10.1126/sciadv.1701593

Mitchell, T. M., & Faulkner, D. R. (2009). The nature and origin of off-fault damage surrounding strike-slip fault zones with a wide range of displacements: A field study from the Atacama fault system, northern Chile. *Journal of Structural Geology*, *31*(8), 802–816. https://doi.org/10.1016/j.jsg.2009.05.002

Mousavi, S. M., Ogwari, P. O., Horton, S. P., & Langston, C. A. (2017). Spatio-temporal evolution of frequency-magnitude distribution and seismogenic index during initiation of induced seismicity at Guy-Greenbrier, Arkansas. *Physics of the Earth and Planetary Interiors*, *267*, 53–66. https://doi.org/10.1016/j.pepi.2017.04.005

Ogwari, P. O., Horton, S. P., & Ausbrooks, S. (2016). Characteristics of induced/triggered earthquakes during the startup phase of the Guy–Greenbrier earthquake sequence in North–Central Arkansas. *Seismological Research Letters*, *87*(3), 620–630. https://doi.org/10.1785/0220150252

Pavlis, G. L., Vernon, F., Harvey, D., & Quinlan, D. (2004). The generalized earthquake-location (GENLOC) package: An earthquake-location library. *Computers & Geosciences*, *30*(9-10), 1079–1091. https://doi.org/10.1016/j.cageo.2004.06.010

Railroad Commission of Texas (2015). Oil and Gas Docket No. 09-0296410, considering whether operation of the Enervest Operating LLC, is causing or contributing to seismic activity in the vicinity of Reno, Parker County, Texas: TXO Exhibit No. 18. Retrieved from http://www.rrc.state.tx.us/media/31023/09-96411-sho-pfd.pdf

Reiter, D., Leidig, M., Yoo, S. H., & Mayeda, K. (2012). Source characteristics of seismicity associated with underground wastewater disposal: A case study from the 2008 Dallas-Fort Worth earthquake sequence. *The Leading Edge*, *31*(12), 1454–1460. https://doi.org/10.1190/tle31121454.1

Reyes, C. G., & West, M. E. (2011). The waveform suite: A robust platform for manipulating waveforms in MATLAB. *Seismological Research Letters*, *82*(1), 104–110. https://doi.org/10.1785/gssrl.82.1.104

Rothert, E., & Shapiro, S. A. (2007). Statistics of fracture strength and fluid-induced microseismicity. *Journal of Geophysical Research*, *112*, B04309. https://doi.org/10.1029/2005JB003

Rubinstein, J. L., & Mahani, A. B. (2015). Myths and facts on wastewater injection, hydraulic fracturing, enhanced oil recovery, and induced seismicity. *Seismological Research Letters*, *86*(4), 1060–1067. https://doi.org/10.1785/0220150067

Savage, H. M., & Brodsky, E. E. (2011). Collateral damage: Evolution with displacement of fracture distribution and secondary fault strands in fault damage zones. *Journal of Geophysical Research*, *116*, B03405. https://doi.org/10.1029/2010JB007665

Scales, M., DeShon, H. R., Magnani, M. B., Walter, J. I., Quinones, L., & Pratt, T. L. (2017). A decade of induced slip on the causative fault of the M_w 4.0 2015 Venus earthquake, northeast Johnson County, Texas. *Journal of Geophysical Research: Solid Earth*, *122*, 7879–7894. https://doi.org/10.1002/2017JB014460

Segall, P., & Lu, S. (2015). Injection-induced seismicity: Poroelastic and earthquake nucleation effects. *Journal of Geophysical Research: Solid Earth*, *120*, 5082–5103. https://doi.org/10.1002/2015JB012060

Stoeckhert, F., Molenda, M., Brenne, S., & Alber, M. (2015). Fracture propagation in sandstone and slate—Laboratory experiments, acoustic emissions and fracture mechanics. *Journal of Rock Mechanics and Geotechnical Engineering*, *7*(3), 237–249. https://doi.org/10.1016/j.jrmge.2015.03.011

Utsu, T. (1978). Estimation of parameter values in formulas for magnitude-frequency relation of earthquake occurrence. *Zisin (Journal of the Seismological Society of Japan), Series*, *2*(31), 367–382.

Vermylen, J., & Zoback, M. D. (2011). Hydraulic fracturing, microseismic magnitudes, and stress evolution in the Barnett Shale, Texas, USA. In *SPE Hydraulic Fracturing Technology Conference*. Society of Petroleum Engineers, doi:https://doi.org/10.2118/140507-MS

Walsh, F. R., & Zoback, M. D. (2015). Oklahoma's recent earthquakes and saltwater disposal. *Science Advances*, *1*(5), e1500195. https://doi.org/10.1126/sciadv.1500195

Weingarten, M., Ge, S., Godt, J. W., Bekins, B. A., & Rubinstein, J. L. (2015). High-rate injection is associated with the increase in US mid-continent seismicity. *Science*, *348*(6241), 1336–1340. https://doi.org/10.1126/science.aab1345

Wiemer, S., & Wyss, M. (2000). Minimum magnitude of completeness in earthquake catalogs: Examples from Alaska, the western United States, and Japan. *Bulletin of the Seismological Society of America*, *90*(4), 859–869. https://doi.org/10.1785/0119990114

Zhou, H. W. (1994). Rapid three-dimensional hypocentral determination using a master station method. *Journal of Geophysical Research*, *99*(B8), 15,439–15,455. https://doi.org/10.1029/94JB00934

Zhou, R., Huang, G. D., Snelling, P., Thornton, M. P., & Mueller, M. (2013). Magnitude calibration for microseismic events from hydraulic fracture monitoring. In *SEG Technical Program Expanded Abstracts 2013* (pp. 2145–2149). Houston, TX: Society of Exploration Geophysicists, 22–27 September. https://doi.org/10.1190/segam2013-0648.1